

DIFF-MF: A Difference-Driven Channel-Spatial State Space Model for Multi-Modal Image Fusion

Yiming Sun, Zifan Ye, Qinghua Hu, *Senior Member, IEEE*, and Pengfei Zhu

Abstract—Multi-modal image fusion aims to integrate complementary information from multiple source images to produce high-quality fused images with enriched content. Although existing approaches based on state space model have achieved satisfied performance with high computational efficiency, they tend to either over-prioritize infrared intensity at the cost of visible details, or conversely, preserve visible structure while diminishing thermal target salience. To overcome these challenges, we propose DIFF-MF, a novel difference-driven channel-spatial state space model for multi-modal image fusion. Our approach leverages feature discrepancy maps between modalities to guide feature extraction, followed by a fusion process across both channel and spatial dimensions. In the channel dimension, a channel-exchange module enhances channel-wise interaction through cross-attention dual state space modeling, enabling adaptive feature reweighting. In the spatial dimension, a spatial-exchange module employs cross-modal state space scanning to achieve comprehensive spatial fusion. By efficiently capturing global dependencies while maintaining linear computational complexity, DIFF-MF effectively integrates complementary multi-modal features. Experimental results on the driving scenarios and low-altitude UAV datasets demonstrate that our method outperforms existing approaches in both visual quality and quantitative evaluation. Our code will be available at https://github.com/ZifanYe-SEU/DIFF_MF.

Index Terms—Infrared-visible image fusion, difference-driven, channel-exchange, spatial-exchange, cross-modal state space scanning.

I. INTRODUCTION

Multimodal image fusion aims to generate high-quality fused images that comprehensively represent scene contents by learning complementary information from two modalities, thereby enhancing the performance of downstream tasks like object detection and semantic segmentation [1]–[3]. Taking infrared-visible image fusion as an example, infrared images provide illumination-independent thermal imaging capabilities that effectively compensate for visible images’ nighttime perception limitations, yet they typically lack texture information for intuitive identification of thermal targets. Visible images exhibit superior imaging quality with rich texture and color details under adequate illumination. This fusion technique has found widespread applications in scenarios like UAV urban inspections and disaster rescue operations.

Yiming Sun, Zifan Ye, and Pengfei Zhu are with the School of Automation, Southeast University, Nanjing 210096, China. Pengfei Zhu is also with the Low-Altitude Intelligence Lab, Xiong'an National Innovation Center Technology Co., Ltd. and Xiong'an Guochuang Lantian Technology Co., Ltd., Hebei 070001, China (e-mail: sunyiming@seu.edu.cn; yezifan@seu.edu.cn; zhupengfei@tju.edu.cn). (Corresponding author: Pengfei Zhu)

Qinghua Hu are with the School of Artificial Intelligence, Tianjin University, Tianjin 300403, China (e-mail: huqinghua@tju.edu.cn).

Recent years have witnessed growing attention on effectively integrating complementary features from different modalities. Various methods have been proposed, including pre-trained CNN-based approaches [4]–[7], autoencoder architectures, GAN frameworks [8], diffusion models [9]–[11], and Transformer [12]–[16] networks. However, these methods face inherent limitations: CNN-based approaches suffer from restricted receptive fields hindering global context capture; autoencoders inherit CNN’s defects while struggling with multimodal complementarity modeling; GANs encounter training instability leading to adversarial learning collapse; diffusion models suffer from inefficient inference due to prolonged training and sampling requirements; Transformer architectures, despite superior global perception, demand excessive computational resources due to quadratic complexity of attention mechanisms. Notably, the emerging Mamba architecture enables global information modeling with linear computational complexity.

While recent Mamba-based fusion methods like Fusion-Mamba [17] and MambaDFuse [18] have emerged to address computational efficiency, they seem to suffer from a cross-modal information imbalance, typically exhibiting a bias towards a single dominant modality. Specifically, Fusion-Mamba [17] fuses multimodal features before SSM learning, potentially diluting modality-specific information. In contrast, MambaDFuse [18] processes each modality independently via SSMs and then fused the features with a static mean-map strategy. This may restricts effective token-level interaction, risking the loss of contextual information. As illustrated in Fig. 1, FusionMamba’s over-fused features are dominated by infrared intensity, weakening the visible texture details of vehicles; meanwhile, MambaDFuse’s lack of interaction fails to highlight the thermal signatures of pedestrians. Unlike existing fusion methods, our method leverages feature discrepancy maps as a feature extraction guidance. This structure forces the network to focus on the unique variations between modalities. Moreover, the channel-wise interaction and spatial token-mixing scanning mechanisms will adequately fuse the cross-modal features, effectively preserving thermal signatures from infrared modality and texture details from visible modality while maintaining optimal edge textures in background regions.

This paper proposes a difference-driven channel-spatial state space model for multimodal image fusion, termed DIFF-MF. The framework is built upon a multimodal feature extraction backbone, enhanced by three dedicated modules: a difference guidance module; a channel-exchange module; and a spatial-exchange module. Specifically, following feature extraction by the backbone, the framework employs a difference guidance

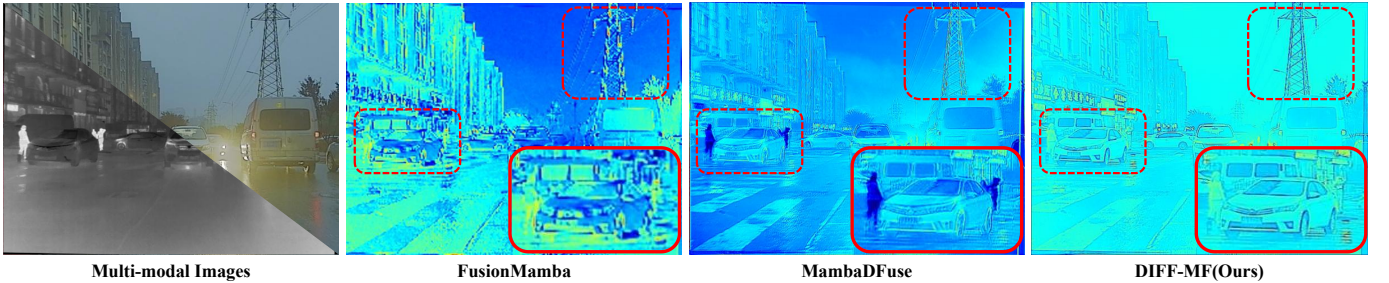


Fig. 1. The feature visualization of different Mamba-based image fusion models. FusionMamba’s over-fused features are dominated by infrared intensity and MambaDFuse’s lack of interaction fails to highlight the thermal signatures of pedestrians. Our DIFF-MF effectively preserves thermal signatures from infrared modality and texture details from visible modality while maintaining optimal edge textures in background regions.

module to perform feature weighting, while a channel-exchange module conducts cross-modal, channel-reweighted state-space exchange for calibration. For spatial processing, we propose three scanning mechanisms operating at different feature scales to capture multiscale spatial information and global cross-modal interactions while maintaining linear complexity. This design enables DIFF-MF to effectively model both channel-wise and spatial global contexts, preserving both modality-specific and cross-modal common features. Our main contributions are summarized as follows:

- We propose a novel differential-driven channel-spatial SSM, which uniquely models both modality-specific differential features and cross-modal collaborative global contexts, leading to superior fusion performance.
- We propose a mechanism for differential feature recalibration and cross-modal channel-exchange reweighting, which balances modality dominance and feature importance through channel-level calibration, thereby achieving equitable representation of multimodal features.
- We design multi-scale cross-modal spatial scanning mechanisms, enabling comprehensive global interaction across feature scales, with extensive experiments validating our method’s state-of-the-art performance in fusion and downstream tasks.

The remainder of the paper is organized as follows: In Section II, we present related work. In Section III, we present our DIFF-MF in detail. We describe extensive experiments in Section IV and conclude the paper in Section V.

II. RELATED WORKS

A. Multi-Modal Image Fusion

Multi-modal image fusion aims to integrate complementary information from different imaging sensors into a single composite image that is more informative and suitable for human perception or subsequent computer vision tasks [19]–[21]. With the advancement of deep learning, a variety of data-driven fusion strategies have been proposed, which can be broadly categorized into the following types:

CNN-based methods constitute one of the earliest and most widely adopted deep learning approaches for image fusion. These methods typically employ convolutional encoders to extract multi-scale features from source images, followed by fusion rules applied in the feature domain. Representative

works include DenseFuse [4], which uses dense connections to enhance feature reuse, and IFCNN [5], a general fusion framework that leverages adaptive fusion strategies. U2Fusion [22] introduced an unsupervised framework that optimizes the similarity between the fused image and source images without requiring ground-truth labels. DIDFuse [23] combined CNN with image decomposition to separate base and detail layers for more robust fusion. Despite their efficiency and ease of training, CNN-based methods are inherently limited by local receptive fields, which restrict their ability to capture long-range dependencies and global contextual information, often leading to suboptimal fusion in complex scenes.

Autoencoder-based frameworks often leverage encoder-decoder architectures to learn compact representations of source images. DeepFuse [24] was among the first to adopt such a structure for image fusion. NestFuse [6] incorporated nested connections and attention mechanisms to enhance feature reuse and highlight salient regions. RFN-Nest [25] further improved feature extraction through residual fusion networks. While autoencoders can effectively compress and reconstruct images, they often inherit the locality constraints of CNNs and may struggle to model complex cross-modal interactions, especially when modalities exhibit significant disparities.

Generative Adversarial Networks (GANs) have been explored to generate fused images with enhanced realism and perceptual quality. FusionGAN [26] use GANs in infrared-visible fusion by employing an adversarial loss to encourage realistic outputs. Subsequent variants like MEF-GAN [27] and MFF-GAN [28] extended the framework to multi-exposure and multi-focus fusion tasks. TarDAL [8] introduced a target-aware dual adversarial learning framework that aligns fusion with downstream detection tasks. However, GAN-based methods are prone to training instability and mode collapse, which can lead to artifacts or loss of detail in the fused output.

Transformer-based methods address the limitations of local modeling by leveraging self-attention mechanisms to capture global dependencies. SwinFusion [13] integrated Swin Transformer blocks into a hierarchical fusion network, enabling cross-scale long-range interaction. CDDFuse [29] combined Transformer with correlation-driven feature decomposition to better separate common and unique features across modalities. EMMA [30] adopted a U-shaped architecture built on Restormer [31] blocks for effective multi-modal fusion. Despite their superior ability to model global contexts, Transformers

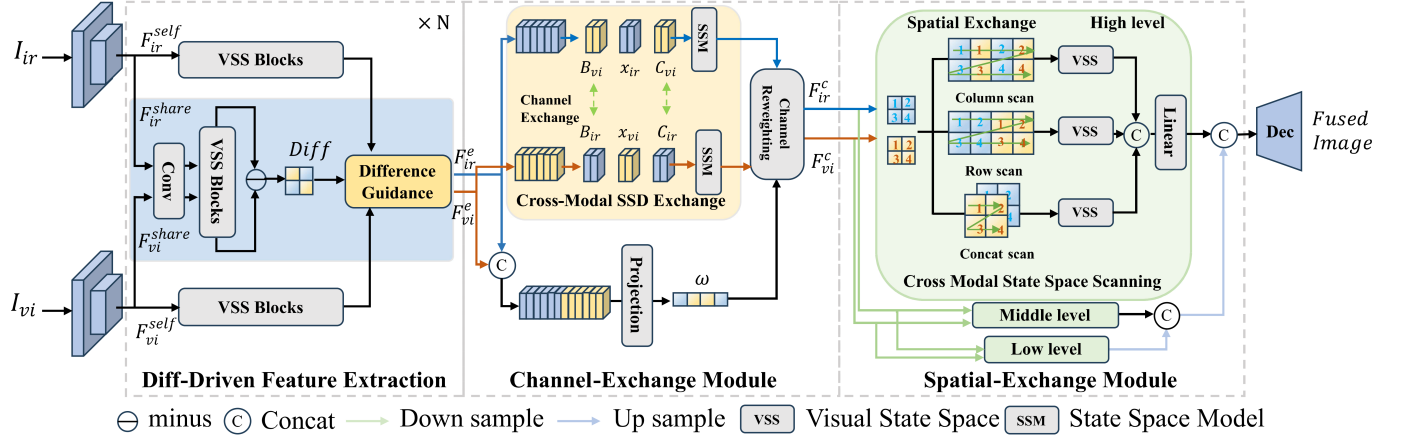


Fig. 2. The architecture of DIFF-MF. DIFF-MF consists of a difference driven feature extraction , a channel-exchange module, and a spatial-exchange module.

suffer from quadratic computational complexity, making them less efficient for high-resolution images, which limits their practicality in real-time applications.

Diffusion models have recently emerged as a powerful generative approach for image fusion. DDFM [9] employed a denoising diffusion process to iteratively refine the fused image, achieving high-quality results. Diff-IF [10] incorporated a fusion knowledge prior to address the lack of ground truth in diffusion training. While diffusion models can achieve high fusion performance, their inference is computationally intensive due to multi-step sampling, hindering deployment in time-sensitive scenarios.

Moreover, there are some other models for image fusion tasks. Huang *et al.* [32] proposed a target-aware image fusion network leveraging Taylor expansion approximation to decompose the images. Li *et al.* [33] adopted graph convolution networks(GCNs) [34] to integrate the graph representation into the infrared and visible fusion. While existing methods have made significant progress, they often trade off between global modeling capability and computational efficiency. Our proposed DIFF-MF seeks to achieve a balance by incorporating a difference-driven dual-branch architecture with channel-spatial state space modules, enabling efficient and effective fusion of multi-modal images.

B. State Space Model

State Space Models(SSMs) [35], developed from modern control theory, can be considered as linear time-invariant(LTI) systems. SSMs are able to capture long-range information by mapping the 1D input $x(t) \in \mathbb{R}^N$ to the output $y(t) \in \mathbb{R}^N$ through a hidden state $h(t) \in \mathbb{R}^N$. This process can be formulated as the following linear ordinary differential equations(ODEs):

$$\begin{aligned} h'(t) &= Ah(t) + Bx(t), \\ y(t) &= Ch(t) + Dx(t), \end{aligned} \quad (1)$$

where $A \in \mathbb{R}^{N \times N}$, $B \in \mathbb{R}^{N \times 1}$, $C \in \mathbb{R}^{N \times 1}$, and $D \in \mathbb{R}^N$ can be regarded as projection matrices. To combined the SSMs with deep learning, the discretization process is applied to Eq.

(1) through a timescale parameter Δ which can discretize the projection matrices $A \in \mathbb{R}^{N \times N}$, $B \in \mathbb{R}^{N \times 1}$ to discrete forms \bar{A} , \bar{B} . Commonly, the zero-order hold rule(ZOH) is used to complete the discretization process. It can be formulated as:

$$\begin{aligned} \bar{A} &= \exp(\Delta A), \\ \bar{B} &= (\Delta A)^{-1} (\exp(\Delta A) - I) \cdot \Delta B. \end{aligned} \quad (2)$$

Then Eq. (1) can be written in discrete form as follows:

$$\begin{aligned} h_k &= \bar{A}h_{k-1} + \bar{B}x_k, \\ y_k &= Ch_k + Dx_k. \end{aligned} \quad (3)$$

Based on Eq. (3), Mamba [36] introduces a selective scan mechanism that turns Δ , B , C into input-dependent parameters.

The state space model can be interpreted as a dual form of the self-attention mechanism in Transformer blocks, constituting a special case of generalized attention [37]. Models defined through a linear-time recurrence usually can derive a quadratic form by expanding the matrix formulation characterizing its linear sequence-to-sequence transformation, while models defined through quadratic-time pairwise interactions can derive a linear form by viewing it as a four-way tensor contraction and reducing in a different order. This is called Structured State Space Duality (SSD) [37] where the C , B , x in the SSM are corresponding to the Q , K , V in the self-attention mechanism. Then, a dual form of cross-attention mechanism can be developed according to the SSD theory.

C. Mamba-based Image Fusion

Due to its ability to efficiently model long-range dependencies, Mamba [36] has been widely adopted and has opened new research avenues in computer vision. Unlike Transformers, which rely on self-attention mechanisms with quadratic complexity, Mamba leverages state space models (SSMs) to capture global context with linear computational complexity. This makes it particularly suitable for high-resolution image processing tasks such as multi-modal image fusion, where both efficiency and global receptive fields are critical.

Several pioneering works have adapted Mamba for vision tasks. Vim [38] applied mamba to the Vision Transformer(ViT) [39], developing a visual backbone based on bidirectional Mamba blocks. VMamba [40] introduced a cross-scan mechanism within its SS2D module to adapt SSMs to 2D image data, allowing effective spatial context aggregation without the computational burden of self-attention. Subsequent studies have further extended Mamba's application to various vision domains: Wang *et al.* [41] integrated SSMs into object detection frameworks, while Xing *et al.* [42] applied Mamba to medical image segmentation, demonstrating its capability in capturing long-range spatial dependencies. Lin *et al.* [43] proposed MTMamba for dense scene understanding, highlighting Mamba's versatility in multi-task learning scenarios.

In the specific domain of multi-modal image fusion, two recent Mamba-based approaches have emerged: FusionMamba [17] and MambaDFuse [18]. FusionMamba employs an efficient SS2D module combined with a cross-modality fusion block to integrate features from different modalities. However, it performs feature fusion before SSM-based processing, which may lead to the dilution of modality-specific characteristics early in the pipeline. On the other hand, MambaDFuse introduces an M3 block to process each modality separately through SSMs, followed by a mean-map-weighted fusion strategy. Although this preserves modality-specific information to some extent, it lacks explicit cross-modal interaction during token-level processing, potentially limiting the model's ability to capture synergistic features.

Despite these advances, existing Mamba-based fusion methods have not fully exploited the potential of SSMs in modeling differential features and facilitating cross-modal token mixing. Effective multi-modal fusion requires not only global context aggregation but also careful handling of modality-specific discrepancies and complementary information. These limitations underscore the need for an approach that explicitly leverages differential guidance and cross-modal state-space interactions.

Our proposed DIFF-MF addresses these gaps by introducing a difference-driven channel-spatial state space model. Unlike prior works, DIFF-MF uses feature discrepancy maps to guide both channel-wise and spatial-wise fusion processes. The channel-exchange module enables dynamic cross-modal reweighting via a dual SSM formulation, while the spatial-exchange module employs multi-scale scanning mechanisms to ensure thorough global integration. By maintaining linear complexity and enabling explicit differential feature modeling, DIFF-MF achieves a better balance between efficiency and fusion quality, as validated by extensive experiments in Section IV.

III. METHODS

A. Overall Architecture

In this paper, we propose an image fusion framework termed DIFF-MF. In Fig. 2, DIFF-MF mainly contains three modules: a difference-driven feature extraction, a channel-exchange module, and a spatial-exchange module. Firstly, we send a pair of infrared image $I_{ir} \in \mathbb{R}^{H \times W \times 1}$ and visible image $I_{vi} \in \mathbb{R}^{H \times W \times 3}$ into the difference-driven feature extraction

module to extract features respectively. Then the extracted features, denoted as F_{vi}^e and F_{ir}^e , are sent into the channel-exchange module to fuse the features in the channel dimension. After that, the fused features, denoted as F_{vi}^c and F_{ir}^c , will enter the spatial-exchange module, which will fuse the features in the spatial dimension. At last, the feature maps fused by the spatial-exchange module can be decoded into the final fused image.

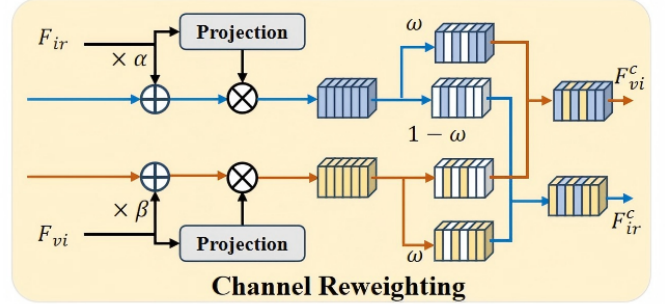


Fig. 3. The architecture of channel reweighting. Parameters α, β are learned from the F_{vi}^e and F_{ir}^e . ω is generated by the Gate Generator.

B. Diff-Driven Feature Extraction

The input features I_{ir} and I_{vi} are processed by two distinct types of dual branches: weight-dependent branches and weight-shared branches. As shown in Fig. 2, the weight-dependent dual branches consist of Visual State Space (VSS) blocks [40] while the weight-shared branches contain CNN blocks and VSS blocks, both of them are weight-shared. Then the output feature maps of weight-dependent dual branches are sent into the difference guidance module to re-weight the feature maps through a difference mask generated by the output of weight-shared dual branches. Let F_{vi}^{self} , F_{ir}^{self} represent the features of the weight-dependent dual branches and F_{vi}^{share} , F_{ir}^{share} represent the features of the weight-shared branches, the entire feature extraction process can be described in Algorithm 1.

Algorithm 1 Diff Driven Feature Extraction

Input: $F_{vi}^{self^n}, F_{ir}^{self^n}, F_{vi}^{share^n}, F_{ir}^{share^n}$ (B, H, W, C)
Output: $F_{vi}^{self^{n+1}}, F_{ir}^{self^{n+1}}, F_{vi}^{share^{n+1}}, F_{ir}^{share^{n+1}}$ (B, H, W, C)

- 1: $F_{vi}^{self^n} \leftarrow VSS(F_{vi}^{self^n})(B, H, W, C)$
- 2: $F_{ir}^{self^n} \leftarrow VSS(F_{ir}^{self^n})(B, H, W, C)$
- 3: $F_{vi}^{share^{n+1}}, F_{ir}^{share^{n+1}} \leftarrow VSS(Conv(F_{vi}^{share^n}, F_{ir}^{share^n}))(B, H, W, C)$
- 4: $Diff \leftarrow \text{Tanh}|F_{vi}^{share^{n+1}} - F_{ir}^{share^{n+1}}|(B, H, W, C)$
- 5: $F_{ir}^{self^{n+1}} \leftarrow (1 - Diff) \odot F_{ir}^{self^n} + Diff \odot F_{vi}^{self^n}$ (B, H, W, C)
- 6: $F_{vi}^{self^{n+1}} \leftarrow (1 - Diff) \odot F_{vi}^{self^n} + Diff \odot F_{ir}^{self^{n+1}}$ (B, H, W, C)
- 7: **return** $F_{vi}^{self^{n+1}}, F_{ir}^{self^{n+1}}, F_{vi}^{share^{n+1}}, F_{ir}^{share^{n+1}}$ (B, H, W, C)

C. Channel-Exchange Module

Channel-exchange module consists of two parts: the cross-modal State Space Duality (SSD) exchange module and the gated-control channel reweighting module. Inspired by [37], the cross-modal SSD exchange module, as shown in Fig 2,

is designed to exchange the channels between the infrared modality and visible modality based on the theories of Structured State Space Duality and SSMs. This exchange method is integrated into the cross-scan mechanism of the VSS blocks. Let F_{vi}^e and F_{ir}^e represent the input feature maps. Consider one route scan as an example. Its first step is formulated as follows:

$$\begin{aligned} T_{ir} &= \text{CrossScan}(F_{ir}^e), \\ T_{vi} &= \text{CrossScan}(F_{vi}^e), \end{aligned} \quad (4)$$

where $T_{ir} \in \mathbb{R}^{B \times L \times C}$ and $T_{vi} \in \mathbb{R}^{B \times L \times D}$ denote the tokens generated from the cross scan. Here B means the batch size, L means the sequence length and C means the channels. Then the tokens are projected into a new channel size for channel exchange and split into x, B, C which are the dual form of $\mathbf{Q}, \mathbf{K}, \mathbf{V}$ in the structured mask attention [37]. It can be represented by the following equation:

$$\begin{aligned} x_{ir}, B_{ir}, C_{ir} &= \text{Split}(\text{Projection}(T_{ir})), \\ x_{vi}, B_{vi}, C_{vi} &= \text{Split}(\text{Projection}(T_{vi})). \end{aligned} \quad (5)$$

After that, these tokens are exchanged and reprojected into the original channel size and then sent into SSMs to learn the fused features. Finally, the output tokens are merged to the original shape:

$$\begin{aligned} F_{vi}^{e'} &= \text{CrossMerge}(\text{SSM}(\text{Projection}[x_{vi}, B_{ir}, C_{ir}]), \\ F_{ir}^{e'} &= \text{CrossMerge}(\text{SSM}(\text{Projection}[x_{ir}, B_{vi}, C_{vi}]), \end{aligned} \quad (6)$$

where $F_{vi}^{e'}$ and $F_{ir}^{e'}$ denote the outputs of the cross-modal SSD exchange module. Then the outputs will be reweighted by the weight parameter $\omega \in \mathbb{R}^{B \times C \times 1}$, which is generated by the gate generator, as shown in Fig. 3. This process can be separated into two parts, the first step can be described as follows:

$$\begin{aligned} F_{ir}^{e''} &= (F_{ir}^{e'} + F_{ir}^e \times \alpha) \odot \text{Projection}(F_{ir}^{e'}), \\ F_{vi}^{e''} &= (F_{vi}^{e'} + F_{vi}^e \times \beta) \odot \text{Projection}(F_{vi}^{e'}), \end{aligned} \quad (7)$$

where α, β are learnable parameters learned from F_{vi}^e and F_{ir}^e , then the temporary features will enter the next reweighting process formulated as follows:

$$\begin{aligned} \omega &= \text{Projection}(\text{Concat}(F_{ir}^e, F_{ir}^{e'})), \\ F_{ir}^c &= (1 - \omega) \odot F_{ir}^{e''} + \omega \odot F_{vi}^{e''}, \\ F_{vi}^c &= (1 - \omega) \odot F_{vi}^{e''} + \omega \odot F_{ir}^{e''}. \end{aligned} \quad (8)$$

D. Spatial-Exchange Module

We employ multi-scale scanning mechanisms in the spatial-exchange module to ensure thorough global integration. Spatial-exchange module consists of three cross-modal State Space Scanning blocks from high-scale level to low-scale level. Inspired by [44], we realign the feature maps into fused feature maps and then send them to the VSS blocks. Consider the feature maps $M_{ir} \in \mathbb{R}^{B \times C \times H \times W}$ and $M_{vi} \in \mathbb{R}^{B \times C \times H \times W}$:

$$\begin{aligned} M_{ir} &= [M_{ir}^1, M_{ir}^2, \dots, M_{ir}^C], \\ M_{vi} &= [M_{vi}^1, M_{vi}^2, \dots, M_{vi}^C]. \end{aligned} \quad (9)$$

The realignment process varies in three different types as follows:

$$\begin{aligned} M_f^{column} &= [M_{ir}^1, M_{vi}^1, M_{ir}^2, M_{vi}^2, \dots, M_{ir}^C, M_{vi}^C], \\ M_f^{row} &= [M_{ir}^1, M_{ir}^2, \dots, M_{ir}^C, M_{vi}^1, M_{vi}^2, \dots, M_{vi}^C], \\ M_f^{concat} &= \text{Concat}(M_{ir}, M_{vi}). \end{aligned} \quad (10)$$

Then the three fused feature maps will enter the VSS blocks and concatenate into one feature map $M_f \in \mathbb{R}^{B \times 3C \times H \times W}$. After that, it will be projected into the original channel size of C and fused with other feature maps from another two scale levels.

E. Loss Function

The loss function follows [13], using SSIM loss \mathcal{L}_{ssim} , texture loss \mathcal{L}_{text} , and intensity loss \mathcal{L}_{int} to constrain the fusion network. The SSIM loss [45] is defined as:

$$\mathcal{L}_{ssim} = w_1 \cdot (1 - \text{ssim}(I_f, I_{ir})) + w_2 \cdot (1 - \text{ssim}(I_f, I_{vi})), \quad (11)$$

here $\text{ssim}(\cdot)$ is the structural similarity operation, and w_1, w_2 are both set as 0.5. SSIM loss is employed to constrain the structural similarity between fused image and source images.

The texture loss can guide the fusion network to preserve as many texture details as possible and is formulated as follows:

$$\mathcal{L}_{text} = \frac{1}{HW} \|\|\nabla I_f| - \max(|\nabla I_{ir}|, |\nabla I_{vi}|)\|_1, \quad (12)$$

where ∇ indicates the Sobel gradient operator, which could measure texture information. $|\cdot|$ represents absolute operation, $\|\cdot\|_1$ the l_1 -norm, and $\max(\cdot)$ refers to the element-wise maximum selection.

The intensity loss can guide the fusion network to capture proper intensity information, it can be defined as follows:

$$\mathcal{L}_{int} = \frac{1}{HW} \|I_f - M(I_{ir}, I_{vi})\|_1, \quad (13)$$

where $M(\cdot)$ is an element-wise aggregation operation, which is associated with the specific fusion scenario.

The whole loss function of the network is a weighted sum of all sub-loss function:

$$\mathcal{L}_{total} = \lambda_1 \mathcal{L}_{ssim} + \lambda_2 \mathcal{L}_{text} + \lambda_3 \mathcal{L}_{int}, \quad (14)$$

where λ_1, λ_2 and λ_3 are the hyper-parameters that control the trade-off of each sub-loss function.

IV. EXPERIMENTS

A. Experimental Setting

Implementation Details. We performed experiments on a computing platform with two NVIDIA A40 GPUs. We used Adam Optimization to update the overall network parameters with the learning rate of 2.0×10^{-5} . The training epoch is set to 46 and the batch size is 4.

Datasets and Partition Protocol. We conducted experiments on three publicly available datasets: (M³FD [8], TNO [46] and DroneVehicle [47]).

M³FD: It contains 4,200 infrared-visible image pairs captured by on-board cameras. We used 3,900 pairs of images for training and the remaining 300 pairs for evaluation.

TABLE I
QUANTITATIVE COMPARISON OF OUR DIFF-MF WITH 7 STATE OF-THE-ART METHODS. **RED** INDICATES THE BEST, **BLUE** INDICATES THE SECOND BEST, AND **CYAN** INDICATES THE THIRD BEST.

Methods	Datasets: M ³ FD Dataset					
	EN↑	SD↑	SF↑	MI↑	VIF↑	AG↑
SwinFusion	6.79	35.84	13.685	2.882	0.774	4.603
TarDAL	6.99	39.1	12.649	2.171	0.598	4.256
DIDFuse	6.77	34.23	12.937	2.889	0.737	4.435
CDDFuse	6.9	37.24	14.776	2.709	0.793	4.862
MambaDFuse	6.77	34.23	12.937	2.889	0.737	4.435
FusionMamba	6.85	37.31	9.278	3.295	0.562	3.393
EMMA	6.92	38.25	15.227	2.644	0.769	5.328
DIFF-MF	7.19	55.09	18.787	3.04	0.825	6.33
Methods	Datasets: TNO Dataset					
	EN↑	SD↑	SF↑	MI↑	VIF↑	AG↑
SwinFusion	6.97	41.34	11.485	2.318	0.74	4.424
TarDAL	7.01	43.52	11.373	2.05	0.612	4.016
DIDFuse	7.18	50.42	12.327	1.761	0.633	4.594
CDDFuse	7.15	46.76	13.229	2.222	0.781	4.775
MambaDFuse	6.98	40.49	10.836	2.417	0.739	4.197
FusionMamba	7.04	47.09	9.419	7.656	0.658	3.707
EMMA	7.25	48.23	12.126	2.062	0.695	4.928
DIFF-MF	7.1	63.03	14.672	2.521	0.836	5.393
Methods	Datasets: DroneVehicle Dataset					
	EN↑	SD↑	SF↑	MI↑	VIF↑	AG↑
SwinFusion	7.4	49.59	19.226	2.072	0.623	7.286
TarDAL	7.27	46.14	15.016	1.926	0.485	5.323
DIDFuse	7.19	57.39	19.533	1.852	0.505	6.776
CDDFuse	7.36	46.73	19.523	2.172	0.642	6.857
MambaDFuse	7.39	47.38	18.417	2.275	0.641	6.968
FusionMamba	7.39	53.89	17.562	2.588	0.597	6.504
EMMA	7.38	46.02	18.063	1.877	0.568	6.944
DIFF-MF	7.52	71.69	22.816	2.402	0.643	8.195

DroneVehicle: It contains 28,439 infrared-visible image pairs captured by UAV cameras. We used 300 image pairs for evaluation.

TNO: We performed evaluation on 55 image pairs.

Note that we test our models on the DroneVehicle and TNO Datasets without retraining.

Evaluation Metrics. We evaluated the performance of the proposed method based on qualitative and quantitative results. The qualitative evaluation is mainly based on the visual effect of the fused image. A good fused image needs to have complementary information from multi-modal images. The quantitative evaluation mainly uses quality evaluation metrics to measure the performance of image fusion. We selected 6 popular metrics, including the entropy (EN) [48], spatial frequency (SF) [49], standard deviation (SD), mutual information (MI) [50], visual information fidelity (VIF) [51], and average gradient (AG) [52]. We also evaluate the performance of the different methods on the typical downstream task, infrared-visible object detection and semantic segmentation.

Competing methods. We compared the 7 state-of-the-art methods on three publicly available datasets (M³FD [8], TNO [46] and DroneVehicle [47]). In these comparison methods, TarDAL [8] is a GAN-based method. DIDFuse [23]

and CDDFuse [29] are deep learning-based image decomposition methods. SwinFusion [13] and EMMA [30] are the Transformer-based methods. MambaDFuse [18] and Fusion-Mamba [17] are the Mamba-based methods.

B. Evaluation on the M³FD dataset

Quantitative Comparisons. Table I presents the results of the quantitative evaluation on the M³FD dataset, where our method achieves the best in 5 metrics and the second best performance in the remaining metrics, respectively. Specifically, our method demonstrates significant advantages in EN, SD, AG, and SF metrics, indicating that the fused results effectively retain abundant texture details and contrast information. Meanwhile, our approach leads in the VIF metric, suggesting our fusion results are more beneficial to the visual perception effect of human eyes. Regarding the MI metric, our fusion results achieve the second best, demonstrating satisfactory capability in preserving source image information.

Qualitative Comparisons.

To better show the superiority of our model, we assigned the color information of the 3-channel visible image to the single-channel fused image through the color space conversion between RGB and YCbCr. As shown in Fig. 4, while all existing methods can reduce the interference of smoke in visible images on fused results, our method not only mitigates smoke effects effectively but also preserves a greater amount of detail and texture information in normal regions. The person in our fused images achieves a balanced enhancement in visibility while maintaining the closest resemblance to the original visible images. Furthermore, compared to other approaches, our method exhibits better performance in preserving texture details in foreground terrain and background buildings.

C. Evaluation on TNO datasets

Quantitative Comparisons. Table I reports the performance of the different methods on the TNO dataset for 6 metrics. Our method achieves the best results in 4 metrics. In particular, our fused results maintain strong performance in the SD, SF, and AG metrics, demonstrating sufficient detail our fused outputs have abundant details. As our results attain the second best performance in MI and the highest score in VIF among compared methods, it means effective preservation of valuable source information and better results with human visual perception.

Qualitative Comparisons. As demonstrated in Fig. 5, our fused images maintain superior detail preservation of contours compared to alternative methods under low-light conditions. Windows of houses and eaves are more clear in our fused results, while foreground features including roads and fences have clear outlines. Furthermore, the luminance distribution in our fused images achieves better alignment with human visual perception than comparative approaches.

D. Evaluation on DroneVehicle datasets

Quantitative Comparisons.

The quantitative results of the different methods on the DroneVehicle dataset are reported in Table I. Our method

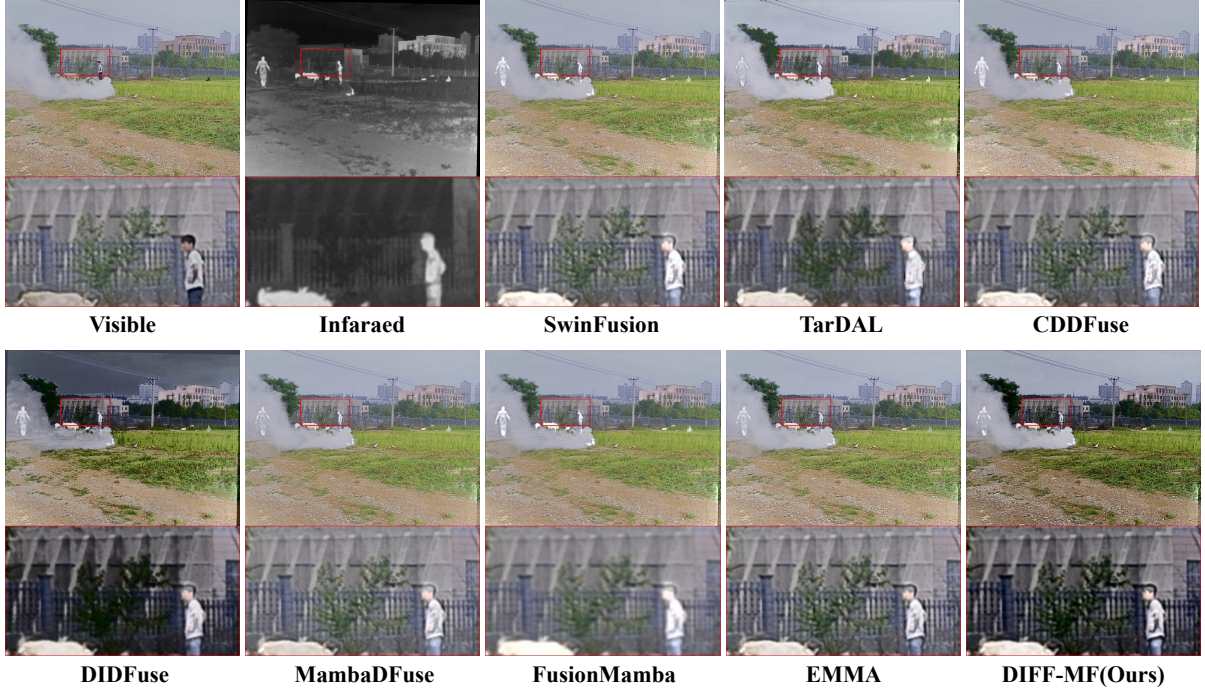


Fig. 4. Qualitative comparisons of various methods on representative images selected from the M³FD dataset.

TABLE II
ABLATION STUDIES ON M³FD DATASET

Methods	Datasets: M ³ FD Dataset					
	EN↑	SD↑	SF↑	MI↑	VIF↑	AG↑
w/o feature extract	5.3	12.48	7.487	2.138	0.484	2.448
w/o channel-exchange	6.8	35.18	13.712	3.347	0.806	4.506
w/o spatial-exchange	6.82	35.46	14.16	3.125	0.853	4.736
w/o difference guidance	6.84	43.49	13.745	2.854	0.738	4.712
DIFF-MF	7.19	55.09	18.787	3.04	0.825	6.33

outperforms all the compared methods on 5 metrics and achieved the second best results on the remaining metric, respectively. Our method achieves the highest score in SD, AG, and SF metrics, indicating effective preservation of substantial texture and edge information in large-scale UAV scenes. While our method is a little bit better than other methods in EN and VIF metrics, these results suggest that our methods can preserve details with human visual perception characteristics. The second-highest MI score further confirms the method's capability in retaining source image information.

Qualitative Comparisons. As shown in Fig. 6, our fused images demonstrate enhanced clarity and superior texture detail preservation relative to existing methods. Magnified views further indicate that while comparative approaches exhibit color noise and ISO noise, our fusion results demonstrate minimal ISO noise presence.

E. Ablation Study

We conducted ablations studies on the M³FD dataset and reported the results in Table II.

Difference Driven Feature Extraction. To verify the effectiveness of difference driven feature extraction module, we first

TABLE III
DIFFERENCE GUIDANCE MODE STUDIES ON M³FD DATASET

Methods	Datasets: M ³ FD Dataset					
	EN↑	SD↑	SF↑	MI↑	VIF↑	AG↑
diff guide v1	7.0	41.59	15.056	3.059	0.77	5.06
diff guide v2	7.12	53.12	17.567	2.434	0.646	5.936
DIFF-MF	7.19	55.09	18.787	3.04	0.825	6.33

remove the overall feature extraction module from DIFF-MF. As shown in Table II, all the metrics show a significant decrease after removing feature extraction, indicating that difference driven feature extraction is can extract features effectively. Then we removed the difference guidance blocks by adding the output feature maps of weighted-share dual branches back to the weighted-dependent dual branches, we found that all the metrics decrease greatly.

Channel-Exchange Module. We removed the channel-exchange module from the DIFF-MF to validate the importance of channel exchanging process. After removal, a decline occurs in 5 metrics. Though the MI performs even better, the models cannot achieve a good balance.

Spatial-Exchange Module. We replaced the spatial-exchange module with a simple averaging method to verify the necessity of the spatial-exchange operation. The results in Table II indicate performance degradation across four evaluation metrics. Although MI and VIF metrics perform better to some extent, the degradation on other metrics is considerable.

F. Qualitative comparisons of Ablation Study.

In this section, we present a qualitative analysis of the fusion results from our ablation study to evaluate the impact

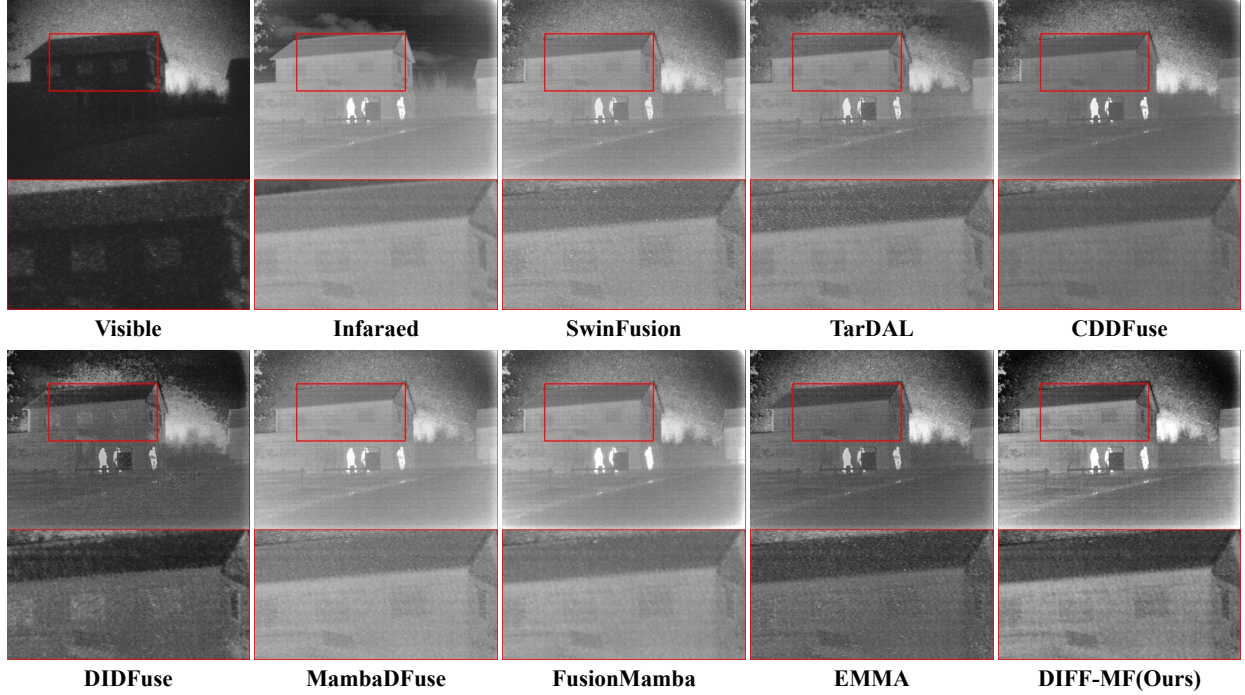


Fig. 5. Qualitative comparisons of various methods on representative images selected from the TNO dataset.

TABLE IV
CHANNEL-EXCHANGE MODULE ABLATION STUDIES ON M³FD DATASET

Methods	Datasets: M ³ FD Dataset					
	EN↑	SD↑	SF↑	MI↑	VIF↑	AG↑
w/o SSD exchange	6.79	35.03	13.087	3.237	0.78	4.38
w/o channel reweighting	7.01	43.04	15.432	3.032	0.759	5.136
DIFF-MF	7.19	55.09	18.787	3.04	0.825	6.33

of different model components. As the results of the model without feature extraction have poor performance, we remove it from this section. As shown in Fig. 7, only DIFF-MF have the best performance while model without difference guidance have excessive contrast losing detail texture information (person in the image). And the results from model without channel-exchange module or without spatial-exchange module is not as clear as the image from DIFF-MF.

G. Analysis and Discussion

Difference Guidance Mode. We changed the guidance mode for further research. Difference guidance version one (diff guide v1) will reweight the feature maps of the visible branch first and then the infrared one, while version two (diff guide v2) will reweight the feature maps in parallelly. The results are shown in Table III, only the version DIFF-MF used performs best indicating that the sequence of the reweighting is related with the fusion results.

SSD Exchange and Channel Reweighting. We also made a further study on the cross modal SSD exchange and channel reweighting, the results shown in Table IV demonstrate that cross modal SSD exchange have a significant impact on the fusion results and channel reweighting is also important.

TABLE V
QUANTITATIVE RESULTS OF DIFFERENT SSD EXCHANGE VERSIONS

Methods	Datasets: M ³ FD Dataset					
	EN↑	SD↑	SF↑	MI↑	VIF↑	AG↑
version 1	6.81	35.39	13.588	3.224	0.78	4.486
version 2	6.81	35.38	13.604	3.283	0.797	4.523
DIFF-MF	7.19	55.09	18.787	3.04	0.825	6.33

1) SSD Exchange Mode. As SSD Exchange can be seen as a dual form of the cross attention of the Transformer block, we change the tokens exchanged between two modals. SSD Exchange version 1 is formulated as follows:

$$\begin{aligned} F_{vi}^{e'} &= \text{CrossMerge}(\text{SSM}(\text{Projection}[x_{vi}, B_{vi}, C_{vi}]), \\ F_{ir}^{e'} &= \text{CrossMerge}(\text{SSM}(\text{Projection}[x_{ir}, B_{vi}, C_{vi}])). \end{aligned} \quad (15)$$

In this process, we only integrate the tokens from visible modal with tokens from infrared modal. In contrast, version 2 only integrate the tokens from infrared modal with tokens from visible modal:

$$\begin{aligned} F_{vi}^{e'} &= \text{CrossMerge}(\text{SSM}(\text{Projection}[x_{vi}, B_{ir}, C_{ir}]), \\ F_{ir}^{e'} &= \text{CrossMerge}(\text{SSM}(\text{Projection}[x_{ir}, B_{ir}, C_{ir}])). \end{aligned} \quad (16)$$

Table V shows the quantitative results of the different cross modal SSD Exchange versions. Only the version of DIFF-MF exchanging both visible modal and infrared modal have the best performance. This may suggest that mutual exchanging can make single modal learn more about the information from another one.

2) Residual Connection of Channel Reweighting Block. We

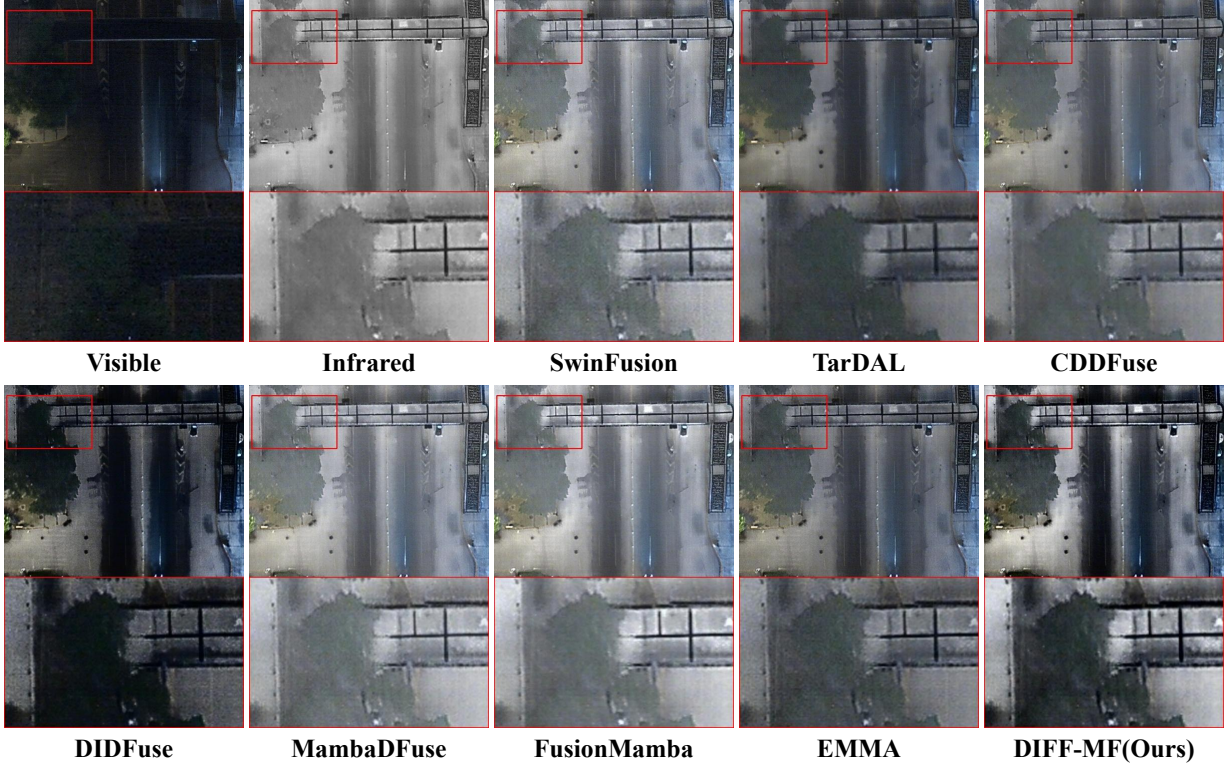
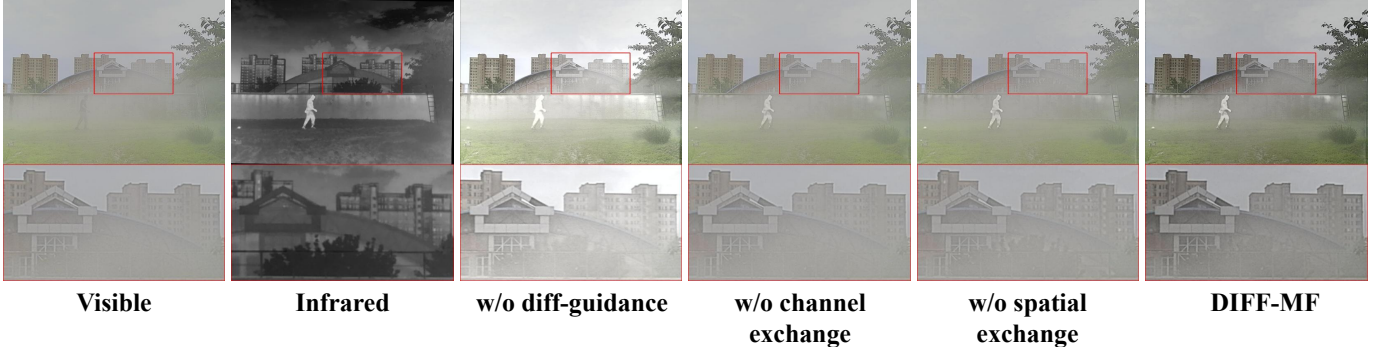


Fig. 6. Qualitative comparisons of various methods on representative images selected from the DroneVehicle dataset.

Fig. 7. Qualitative comparisons of ablation study on representative images selected from the M³FD dataset.TABLE VI
STUDY ON RESIDUAL CONNECTION OF CHANNEL REWEIGHTING BLOCK

Methods	Datasets: M ³ FD Dataset					
	EN↑	SD↑	SF↑	MI↑	VIF↑	AG↑
w/o residual connection	6.78	34.49	13.189	3.249	0.785	4.38
DIFF-MF	7.19	55.09	18.787	3.04	0.825	6.33

make a further study on the channel reweighting block. We have removed the corresponding residual connection reweighting procedure from Eq. 7. The Table VI shows the results of the study, all metrics except the MI have a significant decrease which means our residual connection have a considerable impact on the image fusion results.

Analysis on FLOPs. We make an analysis on the FLOPs of our models. Considering the size of input features is (1,1,512,512)

TABLE VII
STUDY ON FLOPs OF DIFF-MF

Methods	input size	channel size	FLOPs
DIFF-MF using pure transformer	(1,1,512,512)	32	336852.764G
DIFF-MF using SSM	(1,1,512,512)	32	393.871G

and the embedded dimensions is set as 32, we replace all the VSS blocks in our model with the Restormer [31] blocks which is a pure transformer-based model in the computer vision area and its FLOPs is less than the traditional Transformer [53] blocks. The FLOPs of the attention mechanism can be formulated as $4B(HW)^2D$, where B represents the batch size and D represents the embedded dimensions. The H, W is the height and width of the input features. The FLOPs of the VSS blocks can be computed as $4 \times BHW$ where

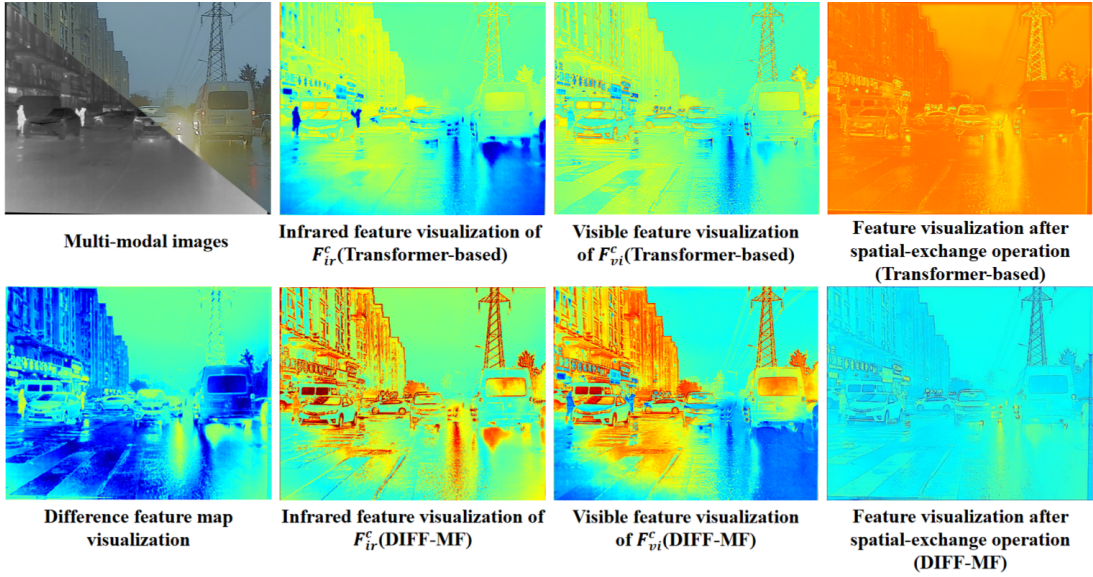
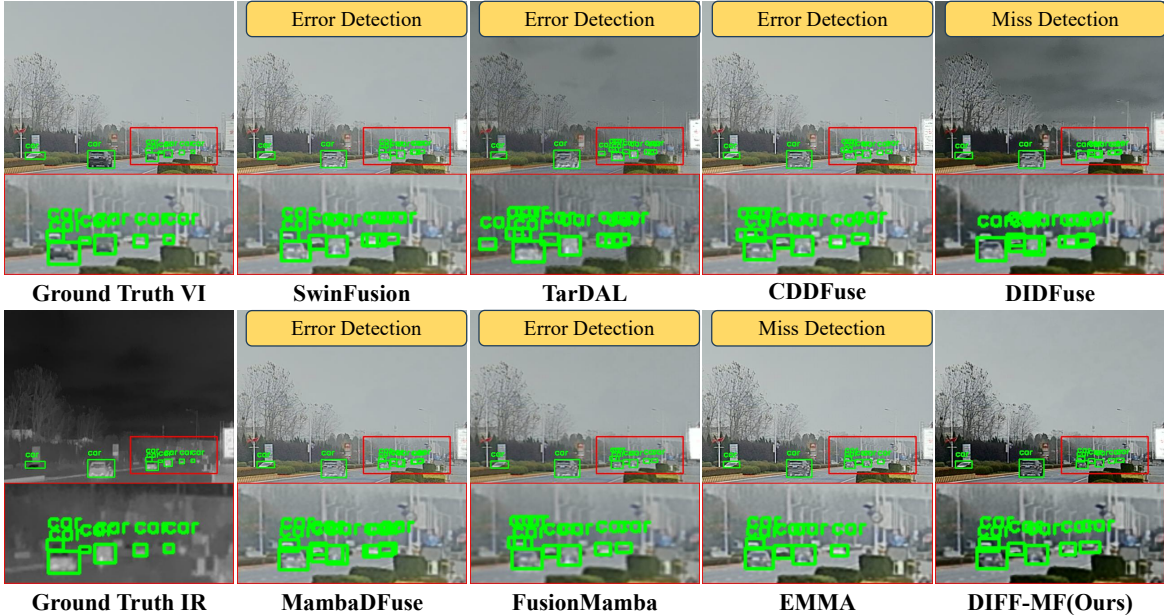
Fig. 8. Feature visualization of selected images from the M³FD dataset.Fig. 9. Qualitative comparisons of various methods on representative images selected from the M³FD dataset.

TABLE VIII
DOWNSTREAM TASK OBJECT DETECTION ON M³FD DATASET

Methods	Datasets: M ³ FD Dataset						
	people	car	bus	lamp	motorcycle	truck	mAP@0.5
SwinFusion	0.751	0.8767	0.8682	0.838	0.7469	0.837	0.8196
TarDAL	0.7588	0.8768	0.9004	0.8605	0.7422	0.839	0.8296
DIDFuse	0.7505	0.8773	0.8899	0.8414	0.7083	0.8577	0.8209
CDDFuse	0.7451	0.8853	0.8954	0.8469	0.7319	0.8681	0.8288
MambaDFuse	0.7597	0.8767	0.9008	0.8529	0.7067	0.8228	0.8199
FusionMamba	0.7575	0.8759	0.8827	0.8644	0.7733	0.8358	0.8316
EMMA	0.7372	0.886	0.8989	0.8526	0.7599	0.8507	0.8309
DIFF-MF	0.7489	0.8853	0.9021	0.8389	0.7533	0.8652	0.8323

4 means the 4 scan routes of the VSS blocks and N is the hidden state of the SSM. We set N as 16 in our models and the numbers of head in Restormer blocks is also set as 16.

Take the FLOPs of other models in the network, the final comparison of the FLOPs is shown in Table VII. It is obvious that the FLOPs of the model using SSM is much less than the model using Restormer. The attention mechanism of Restormer consumes almost 99.8% of the whole models.

Features Visualization. We conducted feature visualization of the feature difference maps. As shown in Fig 8, the difference maps effectively highlight the discrepancies between visible and infrared modality features. Key elements such as people, doorplate lamps, and other light sources are distinctly emphasized in these difference maps. Such emphasis helps the models focus more on these salient regions during the difference-guided learning process. We also present visualizations of the feature

TABLE IX
DOWNSTREAM TASK SEGMENTATION ON FMB DATASET

Methods	Datasets: FMB Dataset															
	Unl	Road	Sidewalk	Building	Traffic light	Traffic sign	Plant	Sky	People	Car	Truck	Bus	Motorcycle	Cycle	Pole	MIoU
SwinFusion	0.214	0.832	0.532	0.762	0.75	0.705	0.827	0.915	0.508	0.733	0.897	0.888	0.907	0.993	0.365	0.722
TarDAL	0.191	0.827	0.545	0.711	0.76	0.682	0.826	0.902	0.516	0.725	0.909	0.878	0.902	0.993	0.307	0.712
DIDFuse	0.207	0.846	0.596	0.749	0.774	0.711	0.827	0.896	0.5	0.745	0.917	0.894	0.908	0.993	0.385	0.73
CDDFuse	0.213	0.842	0.54	0.761	0.747	0.706	0.831	0.91	0.489	0.741	0.903	0.894	0.898	0.993	0.355	0.721
MambaDFuse	0.213	0.844	0.593	0.764	0.771	0.696	0.827	0.916	0.505	0.745	0.91	0.887	0.909	0.993	0.385	0.731
FusionMamba	0.209	0.842	0.559	0.762	0.755	0.7	0.83	0.909	0.516	0.746	0.904	0.882	0.906	0.993	0.384	0.726
EMMA	0.22	0.841	0.579	0.789	0.754	0.711	0.833	0.918	0.474	0.75	0.905	0.899	0.91	0.993	0.399	0.732
DIFF-MF	0.297	0.842	0.612	0.78	0.767	0.711	0.831	0.919	0.527	0.746	0.913	0.903	0.905	0.993	0.408	0.744

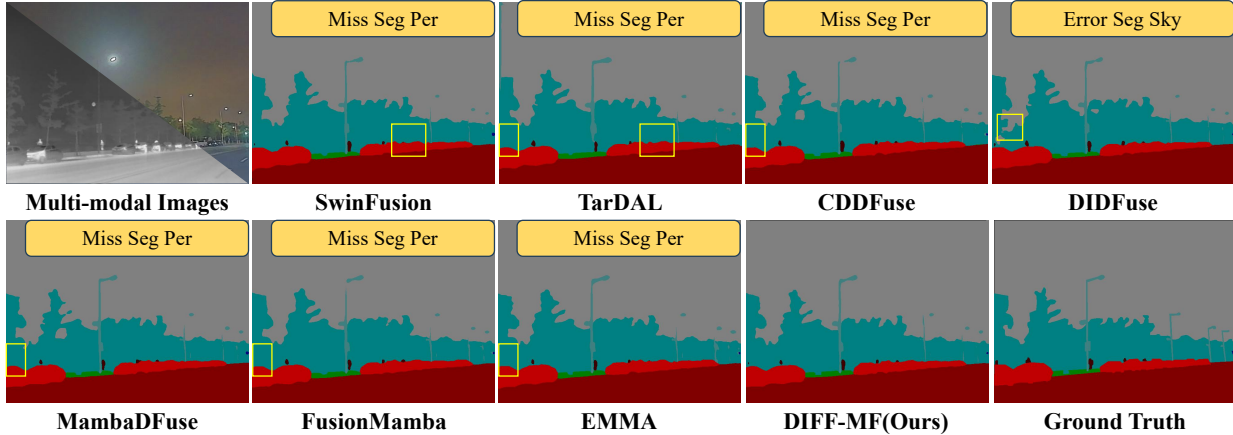


Fig. 10. Qualitative comparisons of various methods on representative images selected from the FMB dataset.

maps generated by the channel-exchange module. Fig 8 reveals a distinct focus: the infrared branch predominantly captures local details such as edges and textures, while the visible branch emphasizes the global context and overall structure. This clear division of representation underscores the complementary of the two modalities. Compared to the Transformer-based method in which we replaced all the VSS blocks with pure transformer blocks, DIFF-MF can capture more details both locally and globally.

In addition, we visualized the feature maps after the spatial-exchange operation. As shown in Fig 8, both models are capable of capturing global features. However, whereas the pure transformer-based model retains some local information, our DIFF-MF model preserves richer fine-grained details, such as the textures of background buildings and vehicles on the road, thereby showcasing the superiority of its difference-aware paradigm.

H. Downstream Task Evaluation

To further study the performance of fusion results in downstream vision tasks, We applied the fused images to multi-modal object detection and multi-modal semantic segmentation. To ensure fairness, we individually re-train the network for each task using fusion results obtained from their own methods.

Object Detection. We conducted the multi-modal object detection task on the M³FD dataset encompassing six categories of labels: people, cars, buses, motorcycles, trucks, and lamps. We split the dataset into training/validation/test sets in an 8 : 1 : 1 ratio. We employed YOLOv5 [54] detector to evaluate

the detection performance with the metric mAP@0.5 [55]. The training epoch is 400, batch size is 8. The optimizer and initial learning rate are set as an SGD optimizer, 1.0×10^{-2} , respectively. Table VIII demonstrates that DIFF-MF achieves the best detection performance. The qualitative comparison results are shown in Fig. 9. On the results of the DIFF-MF are most closely to the Ground Truth, while other results have wrong or missing detection of the car.

Semantic Segmentation. We conducted the MMSS task on the FMB [56] dataset, which consists of 1500 pairs of multi-modal images and encompasses fifteen categories of pixel-level labels: backgrounds, roads, buildings, traffic lights, traffic signs, and so on. We choose DeeplabV3+ [57] as the segmentation network and value the performances through Intersection over Union (IoU). We separate the dataset into training/validation/test sets in an 8 : 1 : 1 ratio. Cross-entropy loss is employed along with the SGD optimizer. The number of epochs is 300 while the batch size and the initial learning rate are set to 4 and 7.0×10^{-3} . The segmentation results are shown in Table IX and Fig. 10, which demonstrate the superior performance of our method.

V. CONCLUSION

In this paper, we present DIFF-MF, a novel difference-driven channel-spatial state space model for multimodal image fusion. By introducing a dual-branch architecture with differential guidance, our method effectively addresses the critical challenge of balancing modality-specific characteristics and cross-modal collaborative features. The proposed channel-

exchange module enables adaptive reweighting of cross-modal features through state space interactions, while the multiscale spatial-scanning mechanism ensures comprehensive modeling of global contextual relationships. Unlike existing approaches that either overlook modality-specific discriminative features or inadequately model cross-scale spatial dependencies, DIFF-MF achieves synergistic integration of infrared thermal signatures and visible texture details while maintaining efficient linear computational complexity. Experimental results demonstrate that our framework successfully preserves critical information from both modalities, offering a robust solution for practical applications requiring reliable scene representation under complex imaging conditions. The proposed methodology not only advances multimodal fusion performance but also provides insights for designing efficient state-space-based architectures in vision tasks.

REFERENCES

- [1] C. Zhao, P. Yang, F. Zhou, G. Yue, S. Wang, H. Wu, G. Chen, T. Wang, and B. Lei, "Mhw-gan: Multidiscriminator hierarchical wavelet generative adversarial network for multimodal image fusion," *IEEE Transactions on Neural Networks and Learning Systems*, vol. 35, no. 10, pp. 13 713–13 727, 2024.
- [2] J. Liu, S. Li, H. Liu, R. Dian, and X. Wei, "A lightweight pixel-level unified image fusion network," *IEEE Transactions on Neural Networks and Learning Systems*, vol. 35, no. 12, pp. 18 120–18 132, 2024.
- [3] Q. Han and C. Jung, "Deep selective fusion of visible and near-infrared images using unsupervised u-net," *IEEE Transactions on Neural Networks and Learning Systems*, vol. 36, no. 3, pp. 4172–4183, 2025.
- [4] H. Li and X.-J. Wu, "Densefuse: A fusion approach to infrared and visible images," *IEEE Transactions on Image Processing*, vol. 28, no. 5, pp. 2614–2623, 2018.
- [5] Y. Zhang, Y. Liu, P. Sun, H. Yan, X. Zhao, and L. Zhang, "Ifcnn: A general image fusion framework based on convolutional neural network," *Information Fusion*, vol. 54, pp. 99–118, 2020.
- [6] H. Li, X.-J. Wu, and T. Durrani, "Nestfuse: An infrared and visible image fusion architecture based on nest connection and spatial/channel attention models," *IEEE Transactions on Instrumentation and Measurement*, vol. 69, no. 12, pp. 9645–9656, 2020.
- [7] F. Zhao, W. Zhao, and H. Lu, "Interactive feature embedding for infrared and visible image fusion," *IEEE Transactions on Neural Networks and Learning Systems*, vol. 35, no. 9, pp. 12 810–12 822, 2023.
- [8] J. Liu, X. Fan, Z. Huang, G. Wu, R. Liu, W. Zhong, and Z. Luo, "Target-aware dual adversarial learning and a multi-scenario multi-modality benchmark to fuse infrared and visible for object detection," in *Proceedings of the IEEE/CVF Conference on Computer Vision and Pattern Recognition (CVPR)*, 2022, pp. 5802–5811.
- [9] Z. Zhao, H. Bai, Y. Zhu, J. Zhang, S. Xu, Y. Zhang, K. Zhang, D. Meng, R. Timofte, and L. Van Gool, "Ddfm: denoising diffusion model for multi-modality image fusion," in *Proceedings of the IEEE/CVF International Conference on Computer Vision*, 2023, pp. 8082–8093.
- [10] X. Yi, L. Tang, H. Zhang, H. Xu, and J. Ma, "Diff-if: Multi-modality image fusion via diffusion model with fusion knowledge prior," *Information Fusion*, vol. 110, p. 102450, 2024.
- [11] Z. Yang, K. Gao, Y. Zhang, X. Zhang, Z. Hu, J. Wang, J. Wang, and W. Li, "Dsfuse: A dual-diffusion structure for feature fidelity infrared and visible image fusion," *IEEE Transactions on Neural Networks and Learning Systems*, 2025.
- [12] H. Zhao and R. Nie, "Dndt: Infrared and visible image fusion via densenet and dual-transformer," in *2021 International Conference on Information Technology and Biomedical Engineering (ICITBE)*. IEEE, 2021, pp. 71–75.
- [13] J. Ma, L. Tang, F. Fan, J. Huang, X. Mei, and Y. Ma, "Swinfusion: Cross-domain long-range learning for general image fusion via swin transformer," *IEEE/CAA Journal of Automatica Sinica*, vol. 9, no. 7, pp. 1200–1217, 2022.
- [14] L. Qu, S. Liu, M. Wang, and Z. Song, "Transmef: A transformer-based multi-exposure image fusion framework using self-supervised multi-task learning," in *Proceedings of the AAAI conference on artificial intelligence*, vol. 36, no. 2, 2022, pp. 2126–2134.
- [15] V. Vs, J. M. J. Valanarasu, P. Oza, and V. M. Patel, "Image fusion transformer," in *2022 IEEE International conference on image processing (ICIP)*. IEEE, 2022, pp. 3566–3570.
- [16] Y. Fu, T. Xu, X. Wu, and J. Kittler, "Ppt fusion: Pyramid patch transformer for a case study in image fusion," *arXiv preprint arXiv:2107.13967*, 2021.
- [17] X. Xie, Y. Cui, T. Tan, X. Zheng, and Z. Yu, "Fusionmamba: Dynamic feature enhancement for multimodal image fusion with mamba," *Visual Intelligence*, vol. 2, no. 1, p. 37, 2024.
- [18] Z. Li, H. Pan, K. Zhang, Y. Wang, and F. Yu, "Mambadfuse: A mamba-based dual-phase model for multi-modality image fusion," *arXiv preprint arXiv:2404.08406*, 2024.
- [19] J. Li, J. Liu, S. Zhou, Q. Zhang, and N. K. Kasabov, "Gesenet: A general semantic-guided network with couple mask ensemble for medical image fusion," *IEEE Transactions on Neural Networks and Learning Systems*, vol. 35, no. 11, pp. 16 248–16 261, 2024.
- [20] G. Xu, C. He, H. Wang, H. Zhu, and W. Ding, "Dm-fusion: Deep model-driven network for heterogeneous image fusion," *IEEE Transactions on Neural Networks and Learning Systems*, vol. 35, no. 7, pp. 10 071–10 085, 2024.
- [21] J. Liu, S. Li, L. Tan, and R. Dian, "Denoiser learning for infrared and visible image fusion," *IEEE Transactions on Neural Networks and Learning Systems*, vol. 36, no. 7, pp. 13 470–13 482, 2025.
- [22] H. Xu, J. Ma, J. Jiang, X. Guo, and H. Ling, "U2fusion: A unified unsupervised image fusion network," *IEEE Transactions on Pattern Analysis and Machine Intelligence*, vol. 44, pp. 502–518, 2022.
- [23] Z. Zhao, S. Xu, C. Zhang, J. Liu, J. Zhang, and P. Li, "Didfuse: Deep image decomposition for infrared and visible image fusion," in *Proceedings of the Twenty-Ninth International Conference on International Joint Conferences on Artificial Intelligence*. ijcai.org, 2020, pp. 970–976.
- [24] K. Ram Prabhakar, V. Sai Srikanth, and R. Venkatesh Babu, "Deepfuse: A deep unsupervised approach for exposure fusion with extreme exposure image pairs," in *Proceedings of the IEEE international conference on computer vision*, 2017, pp. 4714–4722.
- [25] H. Li, X.-J. Wu, and J. Kittler, "Rfn-nest: An end-to-end residual fusion network for infrared and visible images," *Information Fusion*, vol. 73, pp. 72–86, 2021.
- [26] J. Ma, W. Yu, P. Liang, C. Li, and J. Jiang, "Fusiongan: A generative adversarial network for infrared and visible image fusion," *Information Fusion*, vol. 48, pp. 11–26, 2019.
- [27] H. Xu, J. Ma, and X.-P. Zhang, "Mef-gan: Multi-exposure image fusion via generative adversarial networks," *IEEE Transactions on Image Processing*, vol. 29, pp. 7203–7216, 2020.
- [28] H. Zhang, Z. Le, Z. Shao, H. Xu, and J. Ma, "Mff-gan: An unsupervised generative adversarial network with adaptive and gradient joint constraints for multi-focus image fusion," *Information Fusion*, vol. 66, pp. 40–53, 2021.
- [29] Z. Zhao, H. Bai, J. Zhang, Y. Zhang, S. Xu, Z. Lin, R. Timofte, and L. Van Gool, "Cddfuse: Correlation-driven dual-branch feature decomposition for multi-modality image fusion," in *Proceedings of the IEEE/CVF conference on computer vision and pattern recognition*, 2023, pp. 5906–5916.
- [30] Z. Zhao, H. Bai, J. Zhang, Y. Zhang, K. Zhang, S. Xu, D. Chen, R. Timofte, and L. Van Gool, "Equivariant multi-modality image fusion," in *Proceedings of the IEEE/CVF conference on computer vision and pattern recognition*, 2024, pp. 25 912–25 921.
- [31] S. W. Zamir, A. Arora, S. Khan, M. Hayat, F. S. Khan, and M.-H. Yang, "Restormer: Efficient transformer for high-resolution image restoration," in *Proceedings of the IEEE/CVF conference on computer vision and pattern recognition*, 2022, pp. 5728–5739.
- [32] Z. Huang, C. Lin, B. Xu, M. Xia, Q. Li, Y. Li, and N. Sang, "T 2 ea: Target-aware taylor expansion approximation network for infrared and visible image fusion," *IEEE Transactions on Circuits and Systems for Video Technology*, 2025.
- [33] J. Li, L. Bai, B. Yang, C. Li, and L. Ma, "Graph representation learning for infrared and visible image fusion," *IEEE Transactions on Automation Science and Engineering*, 2025.
- [34] A. Micheli, "Neural network for graphs: A contextual constructive approach," *IEEE Transactions on Neural Networks*, vol. 20, no. 3, pp. 498–511, 2009.
- [35] A. Gu, I. Johnson, K. Goel, K. Saab, T. Dao, A. Rudra, and C. Ré, "Combining recurrent, convolutional, and continuous-time models with linear state space layers," *Advances in neural information processing systems*, vol. 34, pp. 572–585, 2021.
- [36] A. Gu and T. Dao, "Mamba: Linear-time sequence modeling with selective state spaces," *arXiv preprint arXiv:2312.00752*, 2023.

- [37] T. Dao and A. Gu, "Transformers are ssms: Generalized models and efficient algorithms through structured state space duality," *arXiv preprint arXiv:2405.21060*, 2024.
- [38] L. Zhu, B. Liao, Q. Zhang, X. Wang, W. Liu, and X. Wang, "Vision mamba: Efficient visual representation learning with bidirectional state space model," *arXiv preprint arXiv:2401.09417*, 2024.
- [39] K. Han, Y. Wang, H. Chen, X. Chen, J. Guo, Z. Liu, Y. Tang, A. Xiao, C. Xu, Y. Xu *et al.*, "A survey on vision transformer," *IEEE transactions on pattern analysis and machine intelligence*, vol. 45, no. 1, pp. 87–110, 2022.
- [40] Y. Liu, Y. Tian, Y. Zhao, H. Yu, L. Xie, Y. Wang, Q. Ye, J. Jiao, and Y. Liu, "Vmamba: Visual state space model," *Advances in neural information processing systems*, vol. 37, pp. 103 031–103 063, 2024.
- [41] Z. Wang, C. Li, H. Xu, and X. Zhu, "Mamba yolo: Ssms-based yolo for object detection," *arXiv preprint arXiv:2406.05835*, 2024.
- [42] Z. Xing, T. Ye, Y. Yang, G. Liu, and L. Zhu, "Segmamba: Long-range sequential modeling mamba for 3d medical image segmentation," in *International Conference on Medical Image Computing and Computer-Assisted Intervention*. Springer, 2024, pp. 578–588.
- [43] B. Lin, W. Jiang, P. Chen, Y. Zhang, S. Liu, and Y.-C. Chen, "Mtmamba: Enhancing multi-task dense scene understanding by mamba-based decoders," in *European Conference on Computer Vision*. Springer, 2024, pp. 314–330.
- [44] H. Chen, J. Song, C. Han, J. Xia, and N. Yokoya, "Changemamba: Remote sensing change detection with spatio-temporal state space model," *IEEE Transactions on Geoscience and Remote Sensing*, 2024.
- [45] Z. Wang, A. C. Bovik, H. R. Sheikh, and E. P. Simoncelli, "Image quality assessment: from error visibility to structural similarity," *IEEE transactions on image processing*, vol. 13, no. 4, pp. 600–612, 2004.
- [46] A. Toet and M. A. Hogervorst, "Progress in color night vision," *Optical Engineering*, vol. 51, no. 1, pp. 010 901–010 901, 2012.
- [47] Y. Sun, B. Cao, P. Zhu, and Q. Hu, "Drone-based rgb-infrared cross-modality vehicle detection via uncertainty-aware learning," *IEEE Transactions on Circuits and Systems for Video Technology*, pp. 1–1, 2022.
- [48] J. Roberts, J. A. N. van Aardt, and F. B. Ahmed, "Assessment of image fusion procedures using entropy, image quality, and multispectral classification," *Journal of Applied Remote Sensing*, vol. 2, 2008.
- [49] A. M. Eskicioglu and P. S. Fisher, "Image quality measures and their performance," *IEEE Trans. Commun.*, vol. 43, pp. 2959–2965, 1995.
- [50] G. Qu, D. Zhang, and P. Yan, "Information measure for performance of image fusion," *Electronics Letters*, vol. 38, pp. 313–315, 2002.
- [51] Y. Han, Y. Cai, Y. Cao, and X. Xu, "A new image fusion performance metric based on visual information fidelity," *Information Fusion*, vol. 14, pp. 127–135, 2013.
- [52] G. Cui, H. Feng, Z. hai Xu, Q. Li, and Y. ting Chen, "Detail preserved fusion of visible and infrared images using regional saliency extraction and multi-scale image decomposition," *Optics Communications*, vol. 341, pp. 199–209, 2015.
- [53] A. Vaswani, N. Shazeer, N. Parmar, J. Uszkoreit, L. Jones, A. N. Gomez, Ł. Kaiser, and I. Polosukhin, "Attention is all you need," *Advances in neural information processing systems*, vol. 30, 2017.
- [54] G. Jocher, A. Stoken, J. Borovec, L. Changyu, A. Hogan, L. Diaconu, F. Ingham, J. Poznanski, J. Fang, L. Yu *et al.*, "ultralytics/yolov5: v3. 1-bug fixes and performance improvements," *Zenodo*, 2020.
- [55] M. Everingham, S. A. Eslami, L. Van Gool, C. K. Williams, J. Winn, and A. Zisserman, "The pascal visual object classes challenge: A retrospective," *International journal of computer vision*, vol. 111, no. 1, pp. 98–136, 2015.
- [56] J. Liu, Z. Liu, G. Wu, L. Ma, R. Liu, W. Zhong, Z. Luo, and X. Fan, "Multi-interactive feature learning and a full-time multi-modality benchmark for image fusion and segmentation," in *Proceedings of the IEEE/CVF international conference on computer vision*, 2023, pp. 8115–8124.
- [57] L.-C. Chen, Y. Zhu, G. Papandreou, F. Schroff, and H. Adam, "Encoder-decoder with atrous separable convolution for semantic image segmentation," in *Proceedings of the European conference on computer vision (ECCV)*, 2018, pp. 801–818.